RSC Advances

ROYAL SOCIETY OF CHEMISTRY

PAPER

View Article Online
View Journal | View Issue

Cite this: *RSC Adv.*, 2025, **15**, 14620

Nd:ZnS@GO nanotubes: a novel adsorbent cum photocatalyst for efficient removal of antibiotics and dyes from wastewater†

Krishan Kumar and Man Singh *

Received 3rd March 2025
Accepted 24th April 2025

DOI: 10.1039/d5ra01504a

rsc.li/rsc-advances

Herein, we designed a novel scaffold of graphene oxide (GO) nanotubes *via* coating of bimetallic neodymium-doped ZnS (Nd:ZnS@GO) for the potential removal of antibiotics and organic fluorescent dyes (OFDs) from wastewater. The GO nanosheets were transformed into nanotubes by unequal charge distribution, which tended them to align in order to minimize surface strain. Nd:ZnS@GO was deployed for fast adsorptive removal of antibiotics and complete photocatalytic degradation (PCD) of OFDs. Nd:ZnS@GO demonstrated superior scavenging efficiency (960 mg g^{-1} for tetracycline and 1117.76 mg g^{-1} for oxytetracycline) compared with previously reported metal-based nanocomposites. The adsorption process followed pseudo-first-order kinetics and the Freundlich isotherm model for both the antibiotics. Benefitting from its fast kinetics, Nd:ZnS@GO could remove pollutants for up to five cycles without losing its adsorption efficiency. The exceptional adsorption capacity was mainly attributed to non-covalent interactions, such as hydrogen bonding, π–π stacking, and cation–π bonding. After adsorption, Nd:ZnS@GO was regenerated and further used for the PCD of tetracycline (TC), oxytetracycline (OTC), methylene blue (MB), brilliant blue-green (BBG), brilliant blue-red (BBR), methyl orange (MO), and quinonoid phenolphthalein (QHIn). This study reveals the synthesis of GO nanotubes as promising and effective adsorbents cum photocatalysts for the adsorption and PCD of OFDs and antibiotics for the first time.

1. Introduction

Over the past few decades, water pollution has emerged as an unavoidable environmental challenge, posing significant threats to aquatic ecosystems, biodiversity, and human health while disrupting socio-economic activities that are reliant on clean water resources.[1,2] The prominent cause of water pollution is the discharge of large amounts of wastewater into the aquatic environment and freshwater bodies.[3] Wastewater from the pharmaceutical industry, including expelled materials and expired medicines, are the main sources of water pollution.[4] Nowadays, antibiotics are used globally as antibacterial drugs for treating diseases in animals and humans. However, only 30% of the medicine is effectively absorbed into the patient's body, and the rest of the drug is excreted through defecation and urinary discharge. This release of antibiotics into water bodies implies a harmful impact on aquatic species and on human health.[5] The TC and OT are most common drugs frequently used for animals as well as human health due to their low cost production and broad activity. Due to the excess production and consumption of TC and OTC, their concentration in aquatic systems has reached up to 20 ppm.[6] The annual consumption of TC is 5500 tons in the U.S. and European countries alone.[7] Continuous release of antibiotics into the aquatic environment leads to antibiotic resistance in microorganisms, which may also lead to incurable diseases. Furthermore, TC and OTC can led to health issues like gastrointestinal diseases, vomiting, and diarrhoea.[8] So, the sequestration of these antibiotics from water is a foremost requirement for the good health of society.

On the same note, broad class of organic fluorescent dyes (OFDs): textiles, dyeing,[9] printing,[10] paper and leather colouring,[11] plastic and polymer colouring, laser technology,[12] optical brighteners in paper and textiles, sensing and detection like chemical sensors, biosensors,[13] environmental monitoring, food quality control, security, and authentication: counterfeit detection, security inks, and coatings,[14] optical authentication.[15] Most OFDs exhibit pleasant bright colours, inhibit sunlight penetration and cause inadequate photosynthesis in aquatic organisms.[16] Excess release of OFDs also hampers the biological (BOD) and chemical oxygen demands (COD) in aquatic plants.[15] Furthermore, they are highly toxic to both animals and humans when consumed at higher concentrations. At present, various extensive methods are used for the removal

---

School of Chemical Sciences, Central University of Gujarat, Sector-30, Gandhinagar, 382030, India. E-mail: Krishan8053649040@gmail.com; Mansingh50@hotmail.com

† Electronic supplementary information (ESI) available: Plots of DLS, BET, SEM, AFM, TGA, PXRD, and tables of ICP-OES and comparative studies. See DOI: https://doi.org/10.1039/d5ra01504a

of pollutants from wastewater, such as adsorption,[17] advanced oxidation,[18] electrochemical degradation,[19] biological degradation,[20] photo-Fenton oxidation,[21] Fenton oxidation ozonation,[21] photocatalysis,[22] and UV treatment.[23] Among them, adsorption and PCD processes are the most promising routes to eliminate pharmaceutical drugs and OFDs from wastewater without generating secondary pollutants in a sustainable manner. Currently, a wide variety of porous adsorbents/photocatalysts like activated carbon,[24] graphene oxide,[25] metal–organic frameworks (MOFs)[26,27] and covalent-organic frameworks (COFs),[16] and nano-scale zero-valent metal oxides[3] are used for the removal and degradation of organic pollutants.[28] However, conventional adsorbents/photocatalysts are limited in their practical application for removing contaminants from wastewater due to their short-term durability, low thermal resistance, lack of biocompatibility, and functionality.[29] In this scenario, nanocomposites of transition metal sulfides with GO garnered noteworthy attention owing to their high thermochemical stability, structural stiffness,[30] and controlled modulation of photo functionalities.[31,32] Qin *et al.*, in 2017, reported ZnS composite with reduced graphene oxides (RGO) for efficient photodegradation of methyl orange.[33] Similarly for the other applications like H_2/O_2 storage[34] effluent adsorption, CO_2 capture,[35] and photocatalysis. Zhigang Li *et al.* and Mufeedah Muringa Kandy *et al.* also reported carbon-based materials as a powerful photocatalyst for hydrogen production and photocatalytic reduction of CO_2 into valuable solar fuels.[36,37] Vikram U. Pandit *et al.* reported a coupled semiconductor photocatalyst of 6,13-pentacenequinone/TiO_2 (PQ/Ti) for the degradation of methylene blue (MB) dye under visible light irradiation.[38,39] However, metal-doped nanotubes (MBNs) represent an emerging class of porous crystalline materials with multifaceted applications.[40,41] They have garnered considerable interest in adsorption and photocatalytic degradation (PCD) studies owing to their exceptional attributes, such as ultra-high porosity,[17] extensive surface area, tunable pore size and geometry, and facile functionalization capabilities.[42] Their well-ordered porous structures and outstanding thermal stability make them excellent candidates for a wide range of applications.[43,44] The functionalization of 2D-GO sheets with novel nanomaterials offers a promising strategy to enhance adsorption and PCD efficiencies.[45] The GO sheets contain oxygenated functional groups such as carboxyl (COOH), aldehyde (CHO), epoxy (COC), and hydroxyl (OH) groups,[42–46] which impart significant potential for applications in catalysis, adsorption, and energy storage due to their high surface area, wide bandgap, and chemical stability.[47,48] Additionally, ZnS's hydrophobic nature and aggregation tendency, combined with the π–π interactions within GO sheets, further enhance the efficient removal of OFDs from aqueous solutions.[49]

In this study, novel bimetallic Nd:ZnS@GO nanotubes have been designed and prepared *via* doping and coating processes. Consequently, the bimetallic ZnS is integrated with GO sheets to form nanotubes, improving their adsorption and PCD performance. Surface-modulated nanotubes have shown potential adsorption behavior with photocatalysis due to their superior semiconductor properties. Nd:ZnS@GO as a semiconductor nanomaterial with higher thermal stability acts as a photosensor for environmental remediation. Moreover, a higher surface-area-to-volume ratio of Nd:ZnS@GO facilitates the maximum adsorption owing to a reduced electron–hole pair recombination rate due to their smaller particle sizes. Therefore, heterostructures are expected to exhibit enhanced adsorption kinetics compared to the bulk nanomaterial. To date, no GO-based nanotubes have been reported for PCD and adsorption of OFDs and antibiotics under visible light. Thus, strategy for GO sheets to GO nanotubes could be a novel contribution due to high capability of morphological transformation through charge induced surface strained wrapping phenomenon.

2. Experimental section

2.1. Materials

Graphite flakes (Gt, <45 μm, ≥99.99%), conc. sulphuric acid (H_2SO_4, 98%), hydrogen peroxide (H_2O_2, ≥85 wt% in H_2O), zinc chloride ($ZnCl_2$, ≥98.9%), neodymium chloride ($NdCl_3$, 99.9%), iron(II) sulfide (FeS, 99.9%), tetracycline (≥98%), oxytetracycline (≥98%), methylene blue (MB, ≥95%), brilliant blue-green (BBG, ≥70%), brilliant blue red (BBR, ≥98%), methyl orange (MO, ≥95%), and phenolphthalein (97%) were procured from Sigma-Aldrich. Potassium permanganate ($KMnO_4$, ≥98%), hydrogen chloride (HCl, 36%), and sodium hydroxide (NaOH, 99%) were obtained from Rankem, petroleum ether (40–60) from SRL, and absolute alcohol (99.9%) from Scvuksmandli Ltd, India.

2.2. Synthesis of zinc sulfide (ZnS)

ZnS was synthesized by following the previously reported methodology.[50] $ZnCl_2$ (50 mg, 0.487 mmol) was dissolved in 100 mL deionized water in a 250 mL round-bottom flask. A NaOH solution (2.5 mmol) was added dropwise with constant stirring at 25 °C. A white precipitate was collected and filtered to obtain $Zn(OH)_2$. ZnS was formed in successive steps by continuously passing H_2S in a solution of $Zn(OH)_2$. ZnS was obtained as a white precipitate after the removal of the residual entities.[51]

2.3. Synthesis of neodymium doped zinc sulfide (Nd@ZnS)

ZnS (20 mg, 0.213 mmol) was homogenized with $NdCl_3 \cdot 6H_2O$ (5 mg, 0.0199 mmol) in 100 mL deionized water and continuously stirred for 12 hours. The resultant material is noted as bimetallic ZnS (Nd@ZnS). The resultant material was washed multiple times with water (3 times) to remove the unreacted residue and dried at 60 °C for three hours (Scheme S1†).

2.4. Synthesis of graphene oxide (GO)

The GO was synthesized from Gt flakes (3.00 g) and $KMnO_4$ (9.00 g) according to a previously reported procedure.[42] An oxidizing mixture of $H_2SO_4 : H_3PO_4$ (8.5 : 1.5 ratio) was poured dropwise in an RB flask placed on an ice bath. The resultant product was stirred at 55 °C at 650 rpm in an oil bath for 12 hours. A mixture of graphite oxide (GtO) was obtained, and icecold water was mixed with the reaction mixture, followed by the addition of 3 mL H_2O_2 (30%) and stirring for 10 min.[52] The resultant product was washed with Milli-Q water, dil. HCl and absolute alcohol, followed by centrifugation at 8000 rpm for 10 min. A brown-colour GtO was extracted in a Petri dish and dried at 60 °C for 12 h. The GO sheet was sonicated for two hours at 28 kHz for exfoliation, and a brownish suspension was obtained (Fig. S1†).

2.5. Synthesis of Nd:ZnS@GO nanotubes

20 mg/100 mL GO and 10 mg/100 mL Nd@ZnS were separately monodispersed to generate cavitation for effective functionalization.[42] Both the solutions were mixed and stirred for 12 h at 60 °C in an RB flask. After mixing, a dark black product settled at the bottom. The obtained product was filtered and washed with copious amounts of ethanol and water, followed by centrifugation at 8000 rpm for 10 min. The black product was dried under vacuum at 80 °C for 12 h. The product formation was confirmed by SEM and HR-TEM analysis (Fig. 3).

$$\mathrm{GO} \cong \rightarrow \mathrm{GO}^*,\ \mathrm{Nd@ZnS} + \mathrm{GO}^* \rightarrow \mathrm{Nd{:}ZnS@GO} \quad (1.0)$$

3. Characterization

UV-visible band spectra were recorded with Shimadzu UV1800 double beam spectrophotometer, X-ray diffraction (XRD) patterns were recorded with Bruker Advance-D8 diffractometer with Cu Kα radiation ($\lambda = 0.15406$ nm, 40 kV, 40 mA), and BET spectra were recorded using a Surfer system-standard, (Thermo Scientific). Thermal stability analysis and DSC were performed by TGA on an EXSTAR TG/DTA 7300 analyzer and a DSC 6000, PerkinElmer, respectively, in a N_2 environment. The morphologies were analysed with HR-TEM and SEM with JEOL JEM 2100 TEM HR LaB6 Version, JEOL, and EVO 18, (Carl Zeiss) respectively. Raman spectra and Atomic Force Microscopy were recorded via VGS, 50–4000 $\mathrm{cm^{-1}}$, 4 K with liquid He and (AFM5100 N) respectively.

3.1. Optimisation of adsorption parameters

Initially, the pH was optimised by varying it from pH 2 to 10 of a 100 ppm solution of TC and OTC by adding an arbitrary amount of adsorbent in 10 mL of the solution. The ideal dose for maximum adsorption was obtained by varying the adsorbent amount from 10 to 30 mg at optimised pH. The adsorption isotherm was evaluated by varying the concentration from 100 to 800 ppm of TC and OTC with the ideal adsorbent dose and pH. Kinetic study for adsorption process of adsorbent was examined its efficiency in the periodic interval of time.

3.2. Adsorption calculation

The amount of the drugs adsorbed on Nd:ZnS@GO surface is noted as adsorption removal capacity. The adsorption efficiency and adsorption capacity (q_e) were calculated by using the following equations:

$$\text{Adsorption efficiency (\%)} = \frac{C_0 - C_e}{C_0} \times 100 \quad (1.1)$$

$$q_e\ (\mathrm{mg\ g^{-1}}) = \frac{C_0 - C_e}{M} \times V \quad (1.2)$$

where C_0 (mg $\mathrm{L^{-1}}$) is the initial concentration and C_e (mg $\mathrm{L^{-1}}$) is the equilibrium concentration of the drugs, while M (g) is the mass of dried drugs, and V (L) is the volume of solution.

$$q_e = \frac{q_t K_L C_e}{1 + C_e K_L} \text{ and } q_e = K_F C_e^{\frac{1}{n}} \quad (1.3)$$

$$\ln(q_e - q_t) = \ln q_e - k_1 t,\ \frac{t}{q_t} = \frac{1}{k_2 {q_e}^2} + \frac{t}{q_e} \quad (1.4)$$

K_L (L $\mathrm{mg^{-1}}$) is the Langmuir equilibrium constant describing the affinity of drugs towards Nd:ZnS@GO. K_F and $1/n$ ($0 < 1/n < 1$) are the Freundlich constant corresponding to the adsorption capacity and linear index, respectively.[53]

3.3. Photocatalytic degradation (PCD) of OFDs *via* using regenerated Nd:ZnS@GO nanotubes

After performing multiple adsorption–desorption cycles, the PCD activity of the regenerated B:ZnS@GO was analysed by conducting PCD experiments of TC, OTC, and OFDs. The PCD experiments were performed with 100 mL (20 ppm) of TC, OTC, QHIn, MB, BBR, BBG, and MO separately by using 1 mg Nd:ZnS@GO photocatalyst under visible light.

3.4. Calculation of quantum yield for OFDs

The degradation rate for OFDs is calculated as

$$\text{Degradation rate (\%)} = \frac{C_0 - C_t}{C_0} \times 100 \quad (1.5)$$

C_0 is the initial OFD concentration at time $t = 0$, and C_t is the concentration of reduced OFDs at t min. The quantum yields for the OFDs were calculated, following our previously reported study.[46] The absorbance of UV-visible band spectra has been used to calculate the quantum yield using Einstein's eqn (1.6):

$$E = mc^2, \quad (1.6)$$

$$\mathrm{Abs} = \varepsilon lc, \quad \Delta c = \frac{\Delta \mathrm{abs}}{\varepsilon l} \quad (1.7)$$

where m is the mass derived from eqn (1.6), Δc is the change in concentration, Δabs is the change in absorbance, and c is the speed of light/photon (3×10^8 m $\mathrm{s^{-1}}$).

4. Results and discussion

The development of bimettalic GO nanotubes was achieved through the charge-induced strained wrapping phenomenon. Nd@ZnS with high surface charge density and enriched Lewis acidic sites electronically interacted with the oxygenated functional groups of GO nanosheets. Nd@ZnS with positive surface charge (+25.61 mV) strongly interacted with the outer surface of the GO sheet (−30.12 mV) *via* coulombic interactions (*vide infra*) (Fig. 1f). Unbalanced charge dipoles induced on GO sheets tend

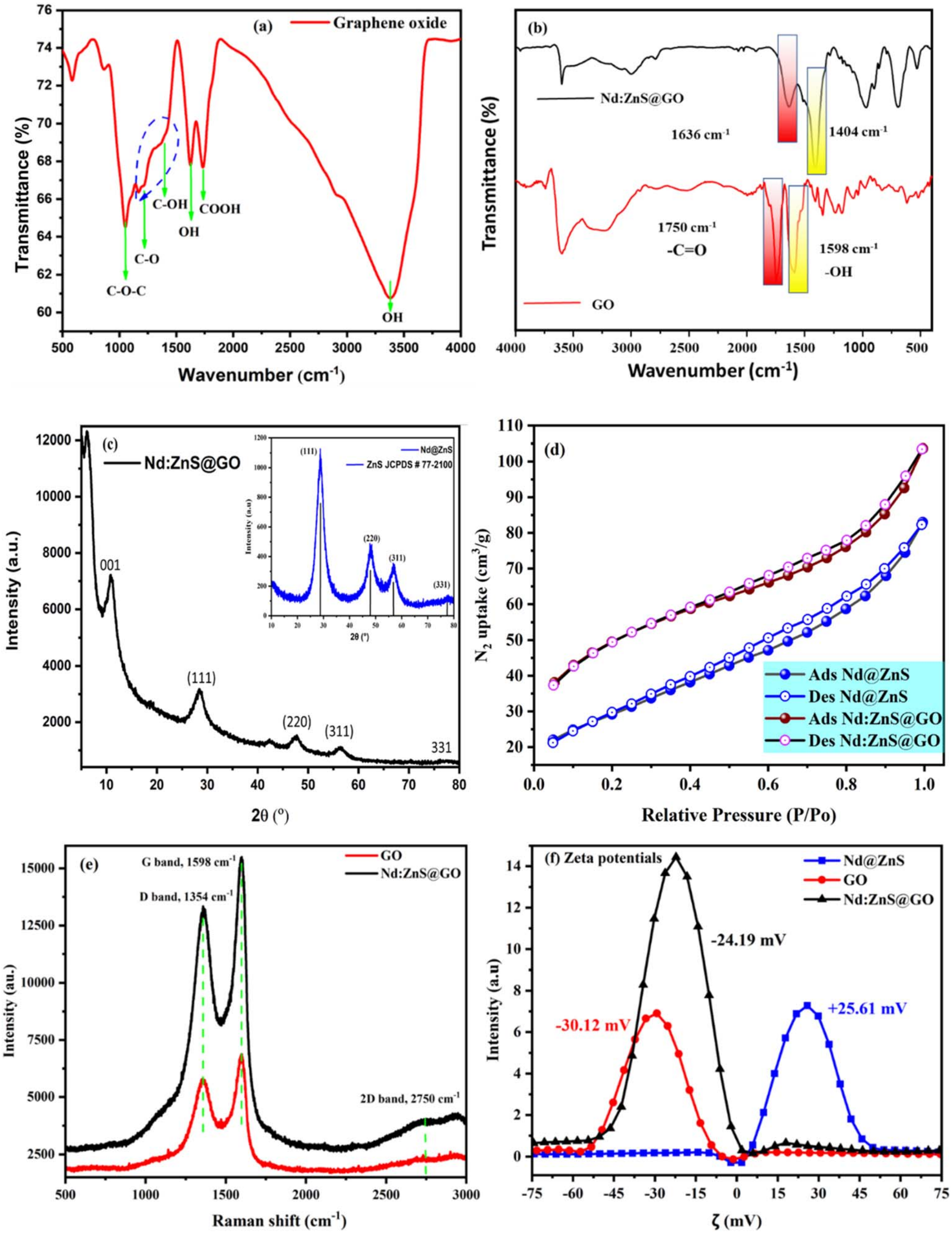

Fig. 1 (a) FT-IR spectrum of GO, (b) comparative FT-IR spectra of GO (red) and Nd:ZnS@GO (black), (c) P-XRD pattern of Nd:ZnS@GO, with the inset showing the P-XRD pattern of Nd@ZnS, (d) comparative N_2 adsorption–desorption isotherm of Nd@ZnS and Nd:ZnS@GO at 77 K, (e) comparative Raman spectrum of GO (red) and Nd:ZnS@GO (black), and (f) comparative zeta potential of GO (red), Nd@ZnS (blue), and Nd:ZnS@GO (black).

to minimize the surface energy *via* restructuring the current morphology. Nd@ZnS composite GO sheets turn into multiwall nanotubes *via* minimizing the charge-induced strain on the surfaces (Scheme S2†). The synthesized material was initially investigated by Fourier transform infrared spectroscopy (FT-IR). The GO, and Nd:ZnS@GO at 1071, 1400, 1250, 1750, and 1626 cm^{-1} ascribed C–O–C, –CHO, >CO, –COOH, and –OH, functional gropus respectively.[42] The broader peak of –OH at 3428 cm^{-1} indicates the free water molecules with GO and Nd:ZnS@GO. The bending vibrations of –OH, epoxide (–O–), and skeletal rings of GO occur at 1626 cm^{-1} with a small stretching vibration hump at 1372 cm^{-1} owing to tertiary C–OH. Nd:ZnS@GO has aligned the FGs to quench the $\pi \rightarrow \pi^*$ transitions and residual potential charges (Fig. 1a and b). Crystallinity and diffraction planes were investigated with X-ray diffraction (XRD). The XRD patterns are broadened with three significant peaks corresponding to the (111), (220), and (311) planes, indicating a standard cubic bulk ZnS lattice, agreeing with standard JCPD card no. 77-2100.[54] The ZnS can be indexed as a cubic zinc blend structure, as its constituents are uniformly distributed on the lattice surfaces. The Nd dopant does not affect the ZnS crystallinity rather than reducing the intensity and broadened the *d*-spacing with similar diffraction peaks and planes (Fig. S2a†). The Gt peak has shifted from 26.2° to 10° and the (002) to (001) plane with GO *via* reducing an interplanar distance of 8.8 Å, attributed to the oxygenated FGs (Fig. S2b†).[48] The Nd@ZnS get coated with the GO sheet on varying the characteristic planes due to the stronger affinities of metal coordination to the functional sites attributed to the wrapping role. Moreover, the ZnS and Nd@ZnS have prevented the aggregation and restacking of the GO sheet due to their good crystallinity, causing the shifting of the significant GO peak. Thus, the Nd@ZnS nanorods are uniformly distributed on GO nanotubes. Broader ZnS peaks showed the size effect of NRs calculated by the Debye–Scherrer equation.

$$D = \frac{0.94\lambda}{\beta \cos \theta} \tag{1.8}$$

where β is the full-width at half maximum (FWHM) intensity and λ is the wavelength. Based on the FWHM of the diffracted peaks of ZnS and Nd@ZnS, the average particle size was ~7 nm. The electrostatic charges around Nd@ZnS have interacted with the FGs and aligned with a symmetric pattern without disrupting the pristine ZnS matrices. Interplanar distances of Nd:ZnS@GO enhanced, unlike ZnS and Nd@ZnS alone. The broadening of the peaks attributed to the mechanical agitation consequently leads to the delamination and exfoliation of the GO sheet (Fig. 1c). After coating with the GO sheet, the structural integrity of Nd:ZnS@GO is maintained due to the exfoliated sheet. However, the intensity of Nd:ZnS@GO has decreased, unlike Nd@ZnS. The porosity of Nd@ZnS and Nd:ZnS@GO was obtained from N_2 adsorption–desorption at 77 K, and the average surface area, pore diameter, and pore volume are 103.177 $m^2\ g^{-1}$, 2.457 nm, and 0.124 cm^3, respectively, for Nd@ZnS and 169.119 $m^2\ g^{-1}$, 1.438 nm and 0.143 cm^3, respectively, for Nd:ZnS@GO, calculated from non-local density functional theory (NLDFT) (Fig. S2c and d†). The isotherms well resemble the IUPAC classification type II isotherm due to macroporous nanorods and nanotubes with sharper edges, hollow cylindrical nanotubes, and broader diameter (Fig. 1d).

The higher N_2 adsorption–desorption with Nd:ZnS@GO infers their higher surface area to accommodate the interstitial cavities. The higher surface area with respect to the pore volume and size depicts structural stability due to doping and coating. The Nd:ZnS@GO with different spacial orientations and charges on the surface, which have further enhanced the N_2-adsorption almost 4 times compared to Nd@ZnS. Raman spectroscopy investigated the defects on GO and Nd:ZnS@GO surfaces. The GO and Nd:ZnS@GO have displayed two major peaks at ~1354 and ~1598 cm^{-1}, consistent with the D and G bands of graphitic C in the GO sheet, respectively. These bands indicate the functionalization of the GO sheet. The D band is due to the disordered states, and the G band shows the stretching vibrational mode E_{2g} from sp^2 of C bonded atoms.[42] Raman band intensity ratio ($I_D/I_G < 1$) indexed as an indicator for estimating the defects in graphitic C of GO sheets.55 The $I_D/I_G < 1$ for Nd:ZnS@GO is higher than that of the pristine GO that predicts an additional defect introduced on the GO surface (Fig. 1e). The ZnS lattice was independently generated by sharper lattice planes with higher intensity. The shifted peaks of GO in Nd:ZnS@GO from 1598 to 1404 cm^{-1} and 1750 to 1636 cm^{-1} indicate an effective functionalization of GO sheets on doping and coating. The residual potential charges of the intensities associated with the Nd@ZnS and GO sheets have ascribed the functionalization of the ZnS lattice. The Nd@ZnS, GO, and Nd:ZnS@GO with +25.61, −30.12, and −24.19 mV surface charges, respectively, analyzed by DLS (Fig. 1f). This has predicted the functionality of the resultant GO nanotubes. Negative surface charges of GO and Nd:ZnS@GO inferred a uniform distribution of oxygenated FGs. The negative surface charge of GO sheet has been accompanied by a accessible morphology towards the electropositive Nd@ZnS with maximum proximity between the oxygenated FGs and Nd@ZnS charge density due uniform electrostatic attraction. The GO sheet with huge oxygenated FGs wrapped the Nd@ZnS as nanotubes. The morphological and structural attributes of Nd:ZnS@GO composite were investigated using SEM analysis. Bifunctional nanomaterials attain a nano-tubular morphology (Fig. 2a and b). EDS and elemental mapping showed all constituent elements of the composite (Fig. 2c and d). In agreement with SEM, HR-TEM analysis also evidenced the distinct formation of graphene oxide nanotubes (Fig. 2). AFM topographical images of GO revealed ~1.5 nm thickness in the selected area from the distribution spectra reported in a previous study.[42] The average roughness of Nd:ZnS@GO was found to be 1.54, indicating the role of doping and coating agents (Fig. S5†). The $\lambda_{max} = 285$ nm of ZnS shifted to $\lambda_{max} = 315$ nm on doping with Nd^{3+}, inferring a symmetric alignment of the dopant throughout the lattice.[56] Hence, the transition of 4f electrons with ZnS lattice at $\lambda_{max} = 315$ nm seems that the S^{2-} strongly attracted towards the Nd^{3+} by facilitating the electronic cloud of ZnS lattice that causing to generate the $\lambda_{max} = 315$ nm with Nd@ZnS (Fig. S2e and f†).

Thermal stability was investigated with TGA/DTG, and weight loss rates were determined for the ZnS, Nd@ZnS, and Nd:ZnS@GO. Thermograms have inferred that enhanced thermal stability is a prerequisite for higher reusability in a photochemical reaction. On increasing the *T*/K, the lattice of catalysts get disrupted on attaining the thermal energy. As the uniformly distributed constituents have been inferred an alignment of 3d and 4f electrons within the matrices. The GO sheet showed sharper weight loss transitions due to uniformly distributed oxygenated FGs onto surfaces.[52] The thermogram of ZnS indicates 47.15, 33.17, and 19.68% weight losses at 104, 596, and 700 °C, respectively, where the 1st weight loss transition is due to moisture, while the 2nd and 3rd transitions are due to disruptions of the main lattice. The 18.96, 26.38, 20.02, and 34.66% weight losses at 100, 300, 391, and 700 °C, respectively, for Nd@ZnS supports the role of the dopant in producing an extra peak. 26.55, 32.37, 20.59, and 20.40% weight losses at 94, 211, 388, and 700 °C, respectively, for Nd:ZnS@GO inferred the role of the coating agent on the Nd@ZnS lattice (Fig. S4†). Thus, the dopant has been uniformly distributed on the ZnS surfaces, supported by FE-SEM (Fig. S3†). The Nd

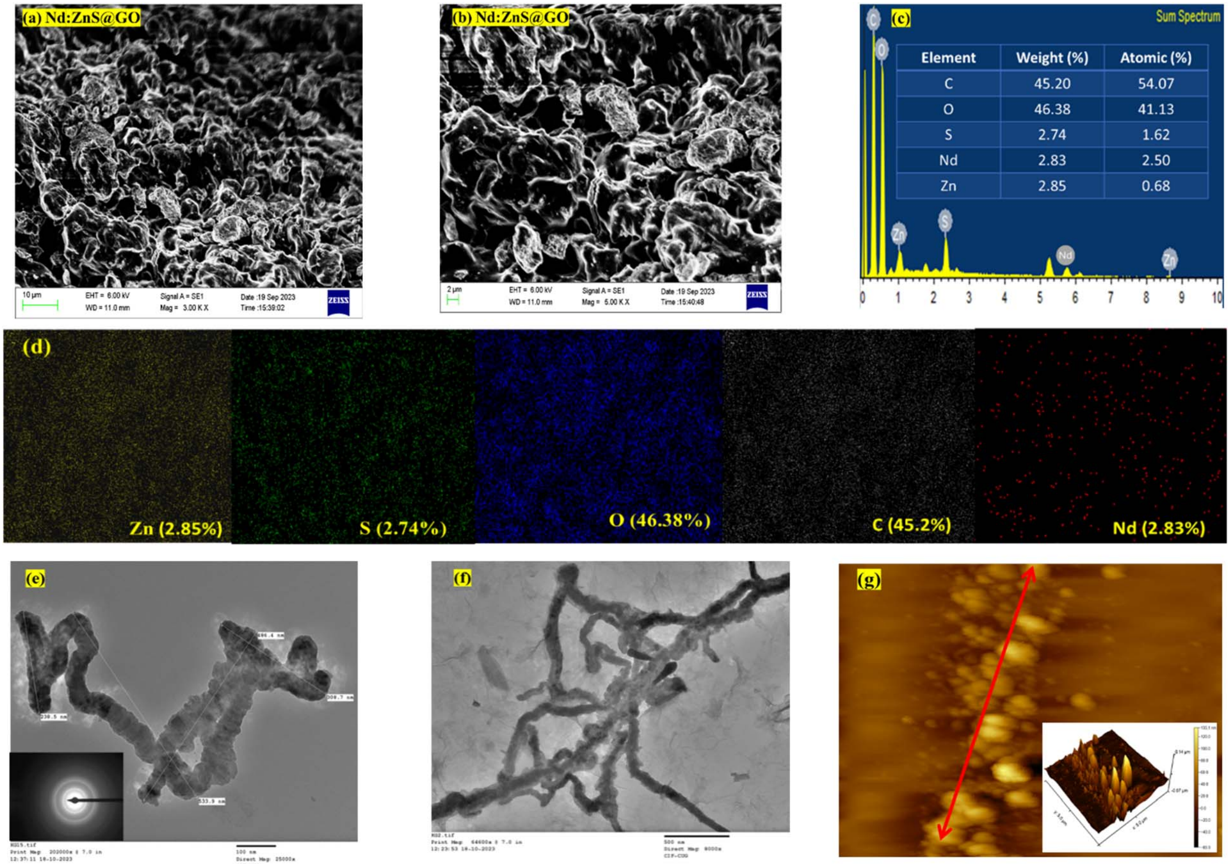

Element	Weight (%)	Atomic (%)
C	45.20	54.07
O	46.38	41.13
S	2.74	1.62
Nd	2.83	2.50
Zn	2.85	0.68

Fig. 2 (a and b) SEM images, (c and d) EDS and elemental mapping, (e and f) HRTEM image with the SAED pattern in the inset, and (g) AFM topographical image with the 3-D perspective of Nd:ZnS@GO in the inset.

dopant has enhanced the ZnS lattice's thermal stability, which favors the enhancement of the reusability.[57] The GO sheet showed a sharp weight loss transition due to uniformly distributed oxygenated FGs.[52] The ZnS, Nd@ZnS, and Nd:ZnS@GO show the Zn compositions of 3.66, 2.595, and 2.506 mg L^{-1}, respectively, while for Nd@ZnS and Nd:ZnS@GO, the Nd compositions are 1.268 and 1.260 mg L^{-1}, respectively. The results show that Nd has been doped and agglomerated with the ZnS lattice (Table S1†).

4.1. Formation of GO nanotubes

The morphological formulation of GO's nanotubes was rationalized through the surface charge-induced-strained wrapping phenomenon and its confirmation was investigated by various instrumental techniques. The 2D-GO nanosheets were transformed into nanotubes after being amalgamated with neodymium-doped ZnS nanorods. This transformation is driven by coulombic interactions, where the negatively charged and polarised surface functional sites of the GO are preferably oriented towards high-density Lewis acidic sites of positively charged Nd@ZnS to minimize the combined surface charge and surface energy.[58] However, upon wrapping the Nd@ZnS nanorods, the strong electrostatic interactions led to a significant change in the spatial morphology shown in Scheme S2.† This study represents the first successful synthesis of GO nanotubes, offering a novel morphological adaptation with enhanced adsorption and photosensing functionality. These nanotubes were subsequently employed in adsorption and photocatalytic degradation experiments targeting TC, OTC, and OFDs in industrial effluents. The GO nanotubes exhibited high efficiency in adsorption and PCD due to their increased surface area, improved charge separation, and structure-function synergism between GO and Nd@ZnS. This innovative approach highlights the potential of using surface charge-induced morphological changes in nanomaterials for improved environmental remediation applications, specifically in the adsorption and degradation of persistent organic pollutants.[59]

4.2. Adsorption studies for tetracycline (TC) and oxytetracycline (OTC)

The adsorptive removal of TC was investigated by a UV-Vis spectrophotometer as TC shows adsorption in the visible range at λ_{max} of 368 nm (Fig. 3a). At the onset, the pH for the adsorption process was tested. As shown in Fig. 3c, the synthesized composite material was able to maximize the adsorption of the drug at around neutral pH. Nonetheless, an increase in the basicity of the solution leads to electrostatic repulsion between anionic forms of the drug and negatively charged nanocomposites, leading to a decrease in adsorption

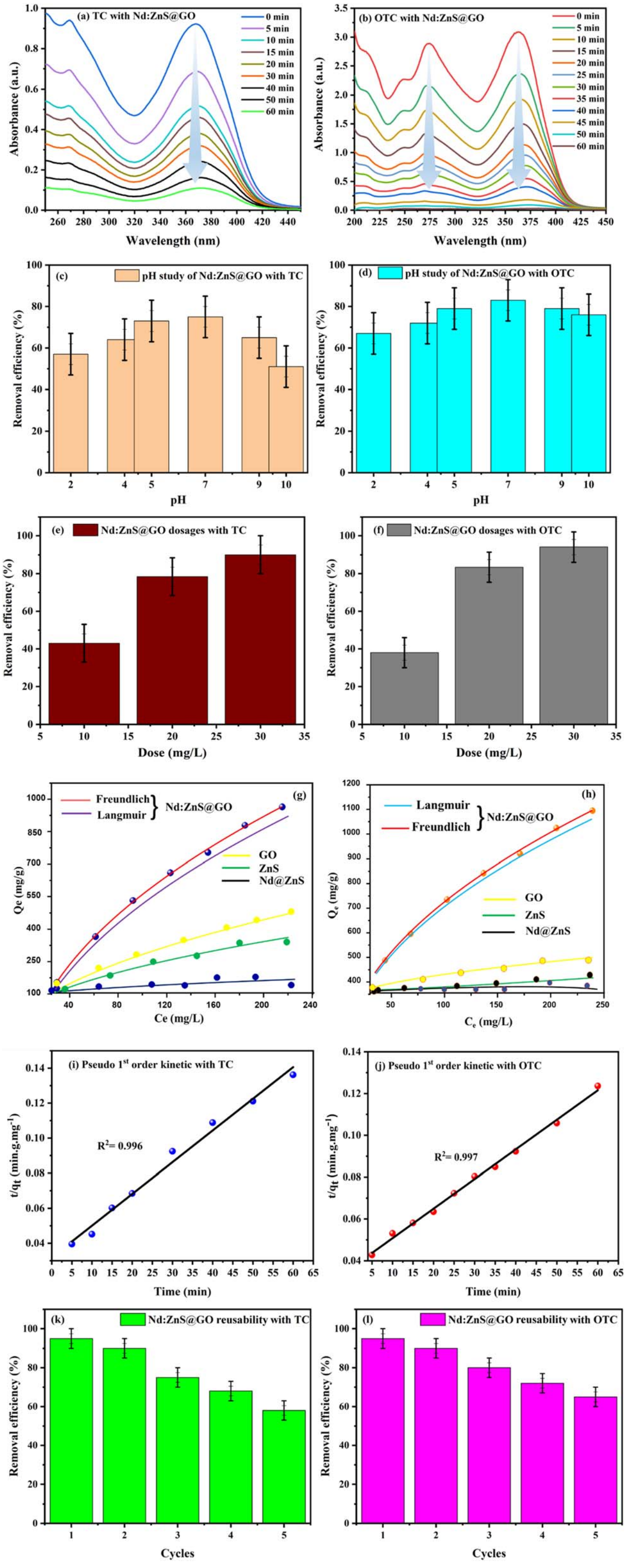

Fig. 3 (a and b) Time dependent UV/Vis spectra, effect of (c and d) pH and (e and f) Nd:ZnS@GO dosage, (g and h) adsorption isotherms, (i and j) pseudo first-order kinetics model, and (k and l) reusability for TC and OTC, respectively.

efficiency. Furthermore, the ideal dose of the adsorbent was optimized at 20 mg L^{-1} (Fig. 3e). The adsorption isotherm for TC was analysed by varying the adsorbate concentration with the optimized dose of the adsorbent (20 mg L^{-1}) and pH of the solution. The maximum adsorption capacity (Q_m) of TC adsorption is 960 mg g^{-1}, which ranks the best among the previously reported values (Fig. 3g and Table S2†). The adsorption isotherm for TC was well established by the Freundlich isotherm on multilayer adsorption with high adsorption capacity even though the electronic charge was balanced. Fast adsorption of TC was attributed to a high kinetic rate constant followed by a pseudo first order mechanism (Fig. 3i). Nanocomposite applicability for water purification was done by multicyclic adsorption desorption behaviour upto five cycles without losing its adsorption efficiency (95%) (Fig. 3k). Similarly, the adsorption of OTC was also investigated by initially optimizing the suitable pH environment to maximize the capacity of the adsorbent by using an UV-Vis spectrophotometer (Fig. 3b and d). The ideal dose of Nd:ZnS@GO for OTC at optimized pH was estimated to be ∼20 mg L^{-1} (Fig. 3f). The maximum adsorption capacity for adsorption of OTC at optimized pH and dose reached up to 1117.76 mg g^{-1}, indicating a superiority of the synthesized nanomaterial. The adsorption process mainly following the Freundlich isotherm indicated a multilayer adsorption process (Fig. 3h). Fast adsorption behavior of the adsorbent was evidenced by its high kinetic rate constant following the pseudo-first order reaction mechanism (Fig. 3j). After maximum adsorption, Nd:ZnS@GO is easily recyclable up to five cycles without losing its adsorption efficiency (Fig. 3l). The adsorption capacity of Nd:ZnS@GO has reached up to 1117.76 mg g^{-1} and 960 mg g^{-1} for OTC and TC, respectively. Nevertheless, ZnS has shown sluggish adsorption behavior due to the dense core lattice of the metal coordination network. Nd@ZnS was also ineffective for the entrapment of targeted pollutants as the void of ZnS was already occupied by Nd. Additionally, GO sheets have shown some adsorption affinity with an adsorption capacity of 420–450 mg g^{-1} for both the antibiotics. This adsorption ability was inferior and might be attributed to the uneven distribution of functional sites and the interaction with the targeted pollutant. Thus, Nd:ZnS@GO nanotube is an excellent adsorbent in graphene chemistry, as both the drugs exhibit 100% removal efficiencies within 45–60 min. Moreover, Nd:ZnS@GO adsorbent dosage (0.05 ± 20 mg L^{-1}) showed a similar behavior with both the antibiotics, attributed to the hydrophilic amide ($CONH_2$), phenolic hydroxyl groups, and hydrophobic diketo substructure with the conjugated rings (Fig. S7†). Thus, the NaCl, KCl, KBr, Na_2SO_4, Na_2CO_3, $MgCl_2$, and $CaCl_2$ using ∼50 fold of each salt that were added to the solutions of antibiotics and Nd:ZnS@GO to examine the influence of metal ions on adsorption. The competitive adsorption experiments revealed that Nd:ZnS@GO had demonstrated remarkable selectivity for antibiotics with a removal efficiency of >98% (Fig. S15†). These salts have slightly (∼0.6%) affected the removal efficiency compared to the results obtained without using salts, which may be due to the screening effect.[6] The salts could not remove water molecules either from the drug or the Nd:ZnS@GO nanotubes with the least change in zeta potential. That widens the adsorption capacity and its recycling ability of wastewater having multiple salts. The experiment demonstrates the strong affinity of drug molecules for the charged Nd:ZnS@GO nanotubes and validates their application prospects. Benefitting from fast kinetics, Nd:ZnS@GO could remove pollutants for up to five cycles without losing its adsorption efficiency. After adsorption experiments were completed, the post-characterization included P-XRD, FT-IR, TGA/DTG, HR-TEM, and EDS (Fig. S6†). These analyses have authenticated the versatility of GO nanotubes. The research work was mainly designated to investigate the effect of doping and coating of ZnS on morphological attributes. The fabricated composite material was fully enriched with multiple polar functionalities on a wide porous network. The practical usability for adsorption of antibiotic pollutants was targeted and thoroughly studied. Nevertheless, the photocatalytic activity was only studied for the regenerated material obtained after multiple adsorption–desorption cycles. After the loss of the ordered architecture, the material was still able to show significant photocatalytic activity.

4.3. Photocatalytic degradation (PCD) of antibiotics and OFDs with regenerated Nd:ZnS@GO nanotubes

After performing multiple adsorption–desorption cycles, the regenerated B:ZnS@GO was deployed for conducting PCD experiments for TC, OTC, and OFDs. The PCD experiments were performed with 100 mL (20 ppm) of TC, OTC, QHIn, MB, BBR, BBG, and MO separately by using 1 mg Nd:ZnS@GO photocatalyst under visible light. 100% degradation of effluents occurred within 1.00–2.00 h (Fig. 4 and S7†). The adsorption and PCD activities were mutually compared, and it was found that Nd:ZnS@GO was bifunctional: acting as an adsorbent cum photocatalyst. Nd:ZnS@GO has generated negative (e^-) and positive (h^+) holes on exposing the photons (visible light) that approaches to the deficient sites of the pollutants and get photodegraded (Fig. 4). Nd:ZnS@GO absorbed photons with energy equal to or greater than the energy difference between the valence and conduction bands on exciting hole pairs for deficient sites.[42] The PCD mechanism of OFDs involves a complex interplay of light absorption on generating e^- and h^+ as charge carriers for redox reactions.[60] Nd:ZnS@GO is exposed to photons; it absorbs the solar energy and excites $e^- \rightarrow h^+$ pairs from the valence to the conduction band. The holes pair of Nd@ZnS in conduction band are transferred to GO sheets, while the holes remain in the Nd@ZnS lattice, facilitating a charge separation for the PCD of pollutants. It allows the GO sheets' electrons to reduce the effluent molecules to their reduced form and settle at the bottom (Fig. 4).

The holes of Nd@ZnS oxidize the water molecules to form hydroxyl radicals ($^{\bullet}OH$), which react with the reduced dye molecules, forming a degraded dye product.[41] Nd:ZnS@GO absorbs solar energy more efficiently and provides a high redox potential to enable the PCD of OFDs. The GO plays an essential role in PCD on account of charge separation, prevents holes from rebounding, and provides a high surface area for photochemical reactions. Nd:ZnS@GO has photodegraded the MB, BBG, BBR, MO, and QHIn with 98, 98.7, 98.2, 97.6, and 98% Φ in 60, 100, 50, 120, and 40 min, respectively. The chemical structure of OFDs influences the reactivity of dyes in the PCD (Fig. S9†).

4.4. Reusability of regenerated Nd:ZnS@GO

The bare Nd:ZnS@GO and with reduced OFDs elucidate the linkages and resultant structural state of dyes. The weight loss and morphology together confirm the overall transitions or structural modifications of Nd:ZnS@GO after PCD (Fig. S11 and S12†). After complete degradation of OFDs, the residue infrared

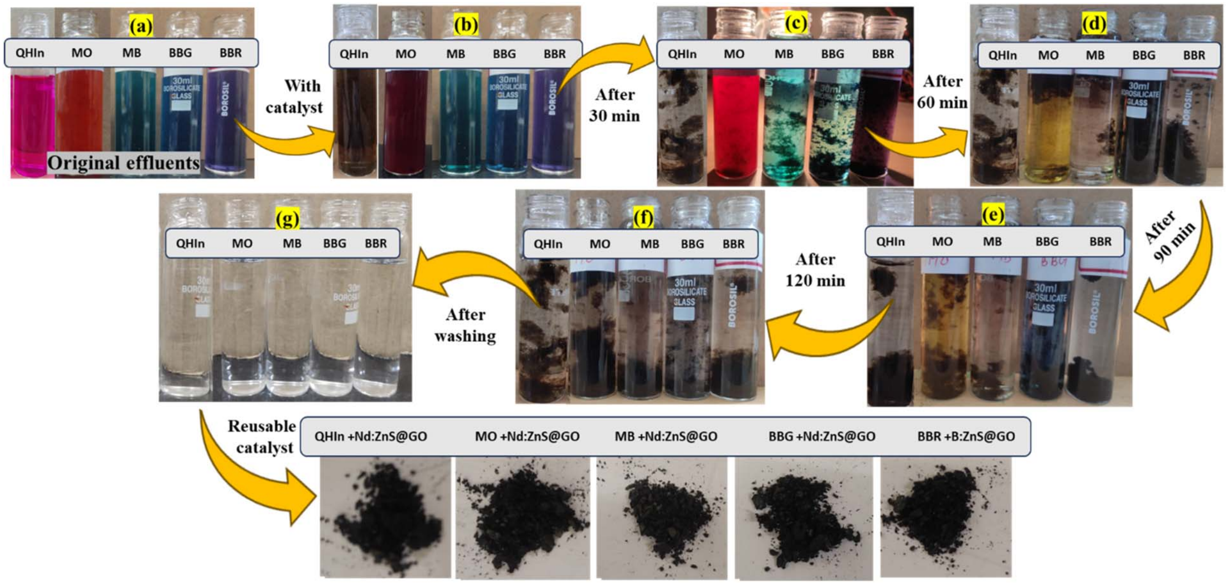

Fig. 4 (a–g) PCD process of OFDs (20 ppm each) using regenerated Nd:ZnS@GO (1 mg) under visible light.

high heat-gaining capacity compared to the pristine Nd:ZnS@GO nanotubes due to engaged functional sites. 26.55, 32.37, 20.59, and 20.40% weight loss at 94, 211, 388, and 700 °C, respectively, for Nd:ZnS@GO inferred mass transitions of lattices before and after PCD. The weight loss before and after PCD elucidates the authenticity of the Nd:ZnS@GO lattice that predict its maximum reusability (Fig. S11†). The PCD activities analysed with FT-IR of bare and reduced OFDs, where the reduced OFDs indicate no characteristic stretching frequency was observed after PCD. The 5-times reusability of Nd:ZnS@GO plays a crucial role in photocatalysis, enhancing adsorption and PCD efficiencies with 99.8–45% yield. After PCD of OFDs, the unaltered morphology and functional sites signify the integrity of Nd:ZnS@GO (Fig. S12 and S13†).

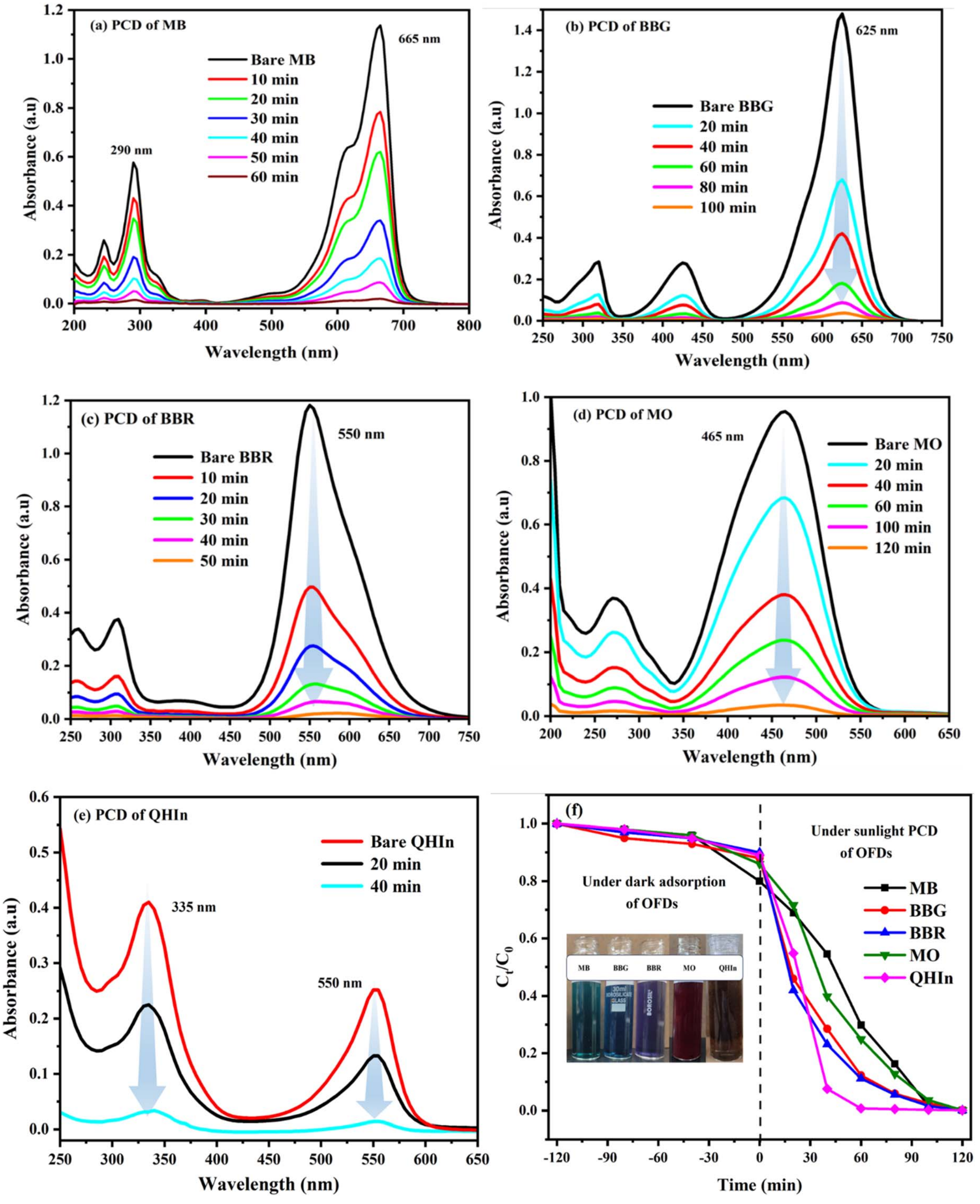

Fig. 5 Photodegradation of (a) MB, (b) BBG, (c) BBR, (d) MO, and (e) QHIn using regenerated Nd:ZnS@GO as the catalyst (f) and PCD kinetics in the dark and in the presence of light.

4.5. Plausible mechanism for antibiotic adsorption

The successful entrapment of antibiotics was thoroughly confirmed by various instrumental analyses. The zeta potential (*ξ*) of composite rapidly decreased due to electrostatic interaction of adsorbate (Fig. S6i†). Moreover, π–π interaction and H-bonding synergistically favored the multilayer adsorption of antibiotic pollutants.[49] The *ξ* of the adsorbent (−24.19 mV) quickly went down to −20.83 mV after TC adsorption and to −13.22 mV after OTC adsorption (Fig. 1f). Even after high ingurgitation of the targeted contaminants, the SEM studies show no structural collapse and support similar morphologies. The comparative EDX analysis before and after the adsorption process shows combined mapping of corresponding elements from the nanotube adsorbent and adsorbates (TC and OTC) (Fig. S6†). The physical and chemical attributes of the nanotube adsorbent after regeneration were also confirmed by several analyses like FT-IR, P-XRD, SEM, HR-TEM, *etc.* Fig. S6b† shows all stretching frequencies of the nanocomposite, supporting high recovery. A similar P-XRD pattern showed structural integrity and regenerated SEM and TEM images revealed the structural robustness as no collapse was observed. Conclusively, a series of experiments well established the bimetallic GO nanotubes as a robust platform for promising capture of antibiotics.

4.6. Plausible mechanism for PCD of OFDs

Adsorption of water-soluble OFDs increases with an increase in hydrophobicity/hydrophilicity due to the wrapped 2D-GO of Nd:ZnS@GO surfaces. The 2D-GO nanosheets have been coated with B@ZnS lattice four to enhance the surface area for maximum PCD. On exposure to sunlight, the valence band electrons of Nd@ZnS get excited to the conduction band. The 2D-GO nanosheets have transferred the photogenerated hole pairs at the interface of Nd@ZnS by resisting recombination. The hole pairs occupying 2D-GO nanosheets and the conduction band of Nd@ZnS can form oxygen-based superoxide radicals ($O_2^{\bullet-}$) (eqn (1.9)). The enhanced PCD activity of the bimetallic nanocomposite was firstly confirmed from EPR spectroscopy. Fig. S14† demonstrates an intense signal after the exposure to the visible light for 10 min and no signal was observed under the dark condition, favourably corroborating the electron hole pair generation under visible light irradiation (Fig. S14†). On protonation, the $O_2^{\bullet-}$ have produced the hydroperoxyl radicals ($HO_2^{\bullet-}$) by generating the hydroxyl radicals ($OH^{\bullet}$) (eqn (2.0)).

The hole pairs present in the valence band of Nd@ZnS acted as an oxidizing agent for oxidizing OFDs.[61] The holes also reacted with adsorbed water molecules and oxygenated the functional groups of 2D-GO nanosheets, producing the $^{\bullet}OH$ (eqn (2.1)). The hole pairs and $^{\bullet}OH$ both interface the deficient sites of OFDs, resulting degradation *via* O_2^- and OH^- ions to OFD molecules by reducing and decomposing the pollutants.[15] The functional sites of OFDs before and after reduction, analyzed with FT-IR, have indicated eco-friendly byproduct residue (Fig. S13†). The OFD molecules containing different numbers of FGs have initiated different reactions, releasing various intermediate products affecting PCD efficiency. The MO, BBG, and BBR dyes possess powerful electron-withdrawing sulfonic groups. The MO, BBG, and BBR dyes show almost the same reactivity for oxidation by hydroxyl radicals.[62] Also, the QHIn and MB having hydroxyl and ketonic groups have increased the resonance and, consequently, the PCD activities. The sulfonic and hydroxyl groups of OFD molecules enabled them to be more reactive in the PCD process (Fig. S9†). The MO shows a milder PCD due to stronger azo and sulphonic groups than the OFDs. The MO and BBG both underwent PCD in 120 and 100 min compared to the MB and BBR in 60 and 50 min, respectively (Fig. 5). The hole pairs generated from Nd:ZnS@GO

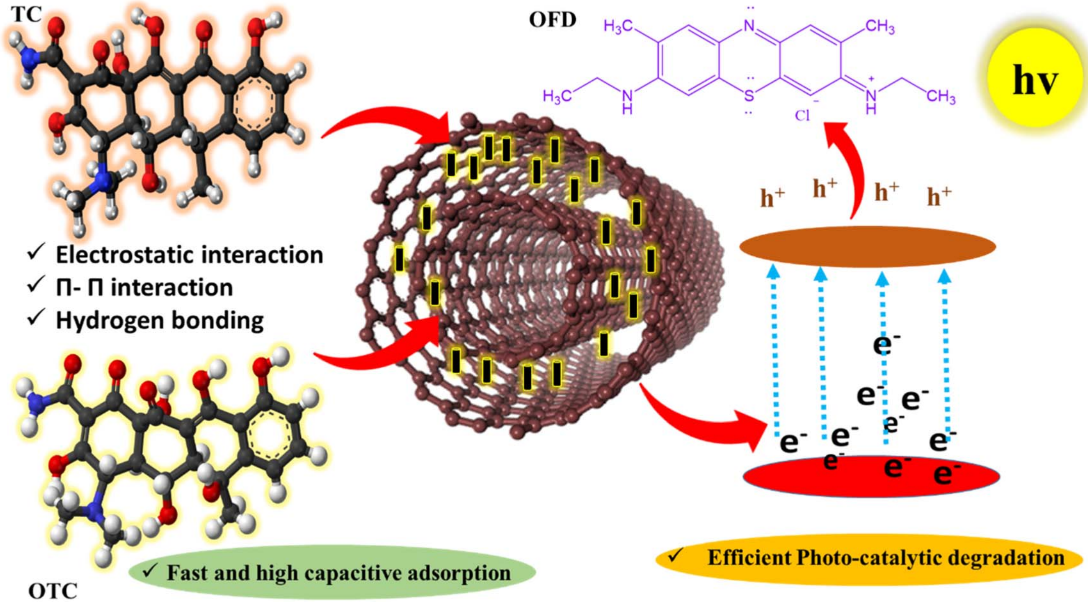

Fig. 6 Plausible mechanism for the adsorption and photocatalytic degradation of pollutants.

have taken longer time with the stronger azo (–NN–) and one SO_3^- of MO and BBG with two SO_3^- and a quaternary nitrogen (N^+–) that causing undesired electron-electron collisions by delaying a PCD process. Thus, the azo-substituted dye is less reactive than sulfonic-substituted dyes in PCD (Fig. S9†). A schematic of the plausible mechanism for PCD of OFDs with B:ZnS@GO is shown in Fig. 6.

$$\text{Nd:ZnS@GO} + h\nu \rightarrow \text{Nd@ZnS(h}^+\text{)} + \text{2D-GO(e}^-\text{)} \quad (1.9)$$

$$\text{O}_2 + \text{2D-GO(e}^-\text{)} \rightarrow + \text{O}_2^{\bullet -} \quad (2.0)$$

$$\text{OH}_2 + \text{Nd@ZnS(h}^+\text{)} \rightarrow {}^{\bullet}\text{OH} \quad (2.1)$$

$$\text{O}_2^{\bullet -} + \text{H}_2\text{O} \rightarrow \text{HO}_2^{\bullet} + \text{OH}^- \quad (2.2)$$

$$\text{2D-GO(e}^-\text{)} + \text{HO}_2^{\bullet} + \text{H}^+ \rightarrow \text{H}_2\text{O}_2 \quad (2.3)$$

$$\text{2D-GO(e}^-\text{)} + \text{H}_2\text{O}_2 \rightarrow {}^{\bullet}\text{OH} + \text{OH}^- \quad (2.4)$$

$$\text{OH}^- + \text{Nd@ZnS(h}^+\text{)} \rightarrow \text{Nd@ZnS} + {}^{\bullet}\text{OH} \quad (2.5)$$

5. Conclusion

A novel nanotubular architecture of graphene oxide (GO), doped with neodymium–zinc sulfide (Nd@ZnS) nanorods, was synthesized to yield a highly functionalized adsorptive-photocatalytic hybrid. The material exhibited exceptional antibiotic adsorption capacities of 960 mg g^{-1} for tetracycline and 1117.76 mg g^{-1} for oxytetracycline, governed by pseudo-first-order kinetics and best described by the Freundlich isotherm model. The oxygenated surface functionalities and nanotubular morphology facilitated selective and multilayer capture of pollutants through hydrogen bonding, π–π stacking, and cation–π interactions. Nd:ZnS@GO retained its adsorption efficiency over five regeneration cycles without significant performance loss. The physical and chemical properties of the nanotube composite were thoroughly verified from a series of experiments. The nanocomposite residue left after saturated adsorption–desorption cycles was further deployed for photocatalytic activity. Owing to their semiconducting nature, the residual nanotubes were able to achieve robust photocatalytic degradation of multiple organic dyes, including methylene blue, brilliant blue-green, brilliant blue-red, methyl orange, phenolphthalein, and both tetracycline derivatives, achieving quantum yields exceeding 90–99%.

Data availability

The data supporting this article have been included as part of the ESI† and is available from the journal site.

Author contributions

Krishan Kumar has conducted the bench work, calculations, frequent discussions, plotting figures and diagrams, experiment observations, exploring new models, and matching with the explored scientific exhalations to create the latest science out of the research substantially. Prof. Man Singh supervised the research work, discussions, and explored new models and outer experiment observations.

Conflicts of interest

The authors confirm that there is no conflict of interest.

Acknowledgements

The authors are thankful to the Central University of Gujarat, India, for its infrastructure and instrumental facilities. Mr Krishan Kumar thanks UGC-DAE CSR Indore (MP) for the financial support (Ref. CRS/2021-22/379) and Dr Mukul Gupta as a Principal Collaborator. Mr Mahesh, CSMCRI-CSIR, Bhavnagar, is acknowledged for scientific and conclusive discussions.

References

1 H. Sereshti, E. Beyrak-Abadi, M. Esmaeili Bidhendi, I. Ahmad, S. Shahabuddin, H. Rashidi Nodeh, N. Sridewi and W. N. Wan Ibrahim, *Nanomaterials*, 2022, **12**, 3576.
2 S. Mohandoss, S. Palanisamy, V. V. Priya, S. K. Mohan, J.-J. Shim, K. Yelithao, S. You and Y. R. Lee, *Microchem. J.*, 2021, **167**, 106280.
3 T. A. Saleh, *Environ. Technol. Innovation*, 2021, **24**, 101821.
4 Z. h. Yang, J. Cao, Y. p. Chen, X. Li, W. p. Xiong, Y. y. Zhou, C. y. Zhou, R. Xu and Y. r. Zhang, *Microporous Mesoporous Mater.*, 2019, **277**, 277–285.
5 W. Xiong, Z. Zeng, G. Zeng, Z. Yang, R. Xiao, X. Li, J. Cao, C. Zhou, H. Chen, M. Jia, Y. Yang, W. Wang and X. Tang, *Chem. Eng. J.*, 2019, **374**, 91–99.
6 Y. Gao, Y. Li, L. Zhang, H. Huang, J. Hu, S. M. Shah and X. Su, *J. Colloid Interface Sci.*, 2012, **368**, 540–546.
7 X. Hou, J. Shi, N. Wang, Z. Wen, M. Sun, J. Qu and Q. Hu, *J. Mol. Liq.*, 2020, **313**, 113512.
8 L. Huang, N. Mao and Q. Shuai, *J. Environ. Chem. Eng.*, 2021, **9**, 104842.
9 S. S. Maktedar, P. Malik, G. Avashthi and M. Singh, *Ultrason. Sonochem.*, 2017, **39**, 208–217.
10 C. I. Vázquez and R. A. Iglesias, *Handb. Nanomater. Ind. Appl.*, 2018, pp. 713–723.
11 I. Khan, K. Saeed, N. Ali, I. Khan, B. Zhang and M. Sadiq, *J. Environ. Chem. Eng.*, 2020, **8**, 104364.
12 G. Xu, F. Liu, J. Lian, N. Wu, X. Zhang and J. He, *Ceram. Int.*, 2018, **44**, 19070–19076.
13 K. Balasubramanian and M. Burghard, *Anal. Bioanal. Chem.*, 2006, **385**, 452.
14 D. A. Nicewicz and T. M. Nguyen, *ACS Catal.*, 2014, **4**, 355–360.
15 R. Gade, J. Ahemed, K. L. Yanapu, S. Y. Abate, Y. T. Tao and S. Pola, *J. Environ. Chem. Eng.*, 2018, **6**, 4504–4513.
16 M. Neem, M. Mondal, R. S. Pillai and S. Neogi, *ACS Appl. Eng. Mater.*, 2024, **2**, 2177–2189.

17 S. K. Sahoo, S. Padhiari, S. K. Biswal, B. B. Panda and G. Hota, *Mater. Chem. Phys.*, 2020, **244**, 122710.

18 H. Rashidi Nodeh, H. Sereshti, E. Beirakabadi and K. Razmkhah, *Int. J. Environ. Sci. Technol.*, 2020, **17**, 819–828.

19 A. Deng, C. Yu, Z. Xue, J. Huang, H. Pan and L. Pei, *J. Mater. Res. Technol.*, 2022, **19**, 1073–1089.

20 A. R. Khataee and M. B. Kasiri, *J. Mol. Catal. A: Chem.*, 2010, **328**, 8–26.

21 C. H. Han, H. D. Park, S. B. Kim, V. Yargeau, J. W. Choi, S. H. Lee and J. A. Park, *Water Res.*, 2020, **172**, 115514.

22 M. E. Borges, M. Sierra, E. Cuevas, R. D. García and P. Esparza, *Sol. Energy*, 2016, **135**, 527–535.

23 D. Chen, D. Wang, Q. Ge, G. Ping, M. Fan, L. Qin, L. Bai, C. Lv and K. Shu, *Thin Solid Films*, 2015, **574**, 1–9.

24 R. Jain, M. Mathur, S. Sikarwar and A. Mittal, *J. Environ. Manage.*, 2007, **85**, 956–964.

25 C. Marin, PhD thesis, Barcelona U, 2018-01-30, University of Barcelona, 2016.

26 M. Abdullah, M. M. Alanazi, S. A. M. Abdelmohsen, S. D. Alahmari, S. Aman, A. Sadaf, A. G. Al-Sehemi, A. M. A. Henaish, Z. Ahmad and H. M. T. Farid, *Mater. Sci. Eng., B*, 2024, **301**, 117207.

27 D. D. Pathak, M. Neem, G. Kumar, B. Modak, S. Neogi and B. P. Mandal, *J. Energy Storage*, 2025, **117**, 116176.

28 F. Fatahi, S. Farhadi, A. Zabardasti and F. Mahmoudi, *Inorg. Chem. Commun.*, 2024, **162**, 112231.

29 P. P. Mondal, M. Neem, R. Chand, A. Pandit and S. Neogi, *Chem. Mater.*, 2024, **36**, 10451–10473.

30 Y. Hanifehpour, B. Soltani, A. R. Amani-Ghadim, B. Hedayati, B. Khomami and S. W. Joo, *J. Ind. Eng. Chem.*, 2016, **34**, 41–50.

31 M. Yudasaka, S. Iijima, V. H. Crespi, A. Jorio, G. Dresselhaus and M. S. Dresselhaus, *Carbon Nanotubes*, 2008, **111**, 605–629.

32 T. Wu, H. Zheng, Y. Kou, X. Su, N. R. Kadasala, M. Gao, L. Chen, D. Han, Y. Liu and J. Yang, *Microsyst. Nanoeng.*, 2021, **7**, 23.

33 S. Patel, S. Mukherjee, M. Neem, S. Neogi, K. L. Ameta, A. Mishra, M. P. Deshpande and M. K. Mishra, *Colloids Surf., C*, 2024, **2**, 100047.

34 Y. Qin, Z. Sun, W. Zhao, Z. Liu, D. Ni and Z. Ma, *Nano-Struct. Nano-Objects*, 2017, **10**, 176–181.

35 M. Neem, P. P. Mondal, A. S. Palakkal and S. Neogi, *Chem. Eng. J.*, 2025, **504**, 158981.

36 Z. Li, K. Li, P. Du, M. Mehmandoust, F. Karimi and N. Erk, *Chemosphere*, 2022, **308**, 135998.

37 M. M. Kandy, *Sustainable Energy Fuels*, 2020, **4**, 469–484.

38 V. U. Pandit, S. S. Arbuj, Y. B. Pandit, S. D. Naik, S. B. Rane, U. P. Mulik, S. W. Gosavi and B. B. Kale, *RSC Adv.*, 2015, **5**, 10326–10331.

39 V. Jawale, A. Al-Fahdawi, S. Salve, S. Pandit, G. Dawange, G. Gugale, M. Chaskar, D. Hammiche, S. Arbuj and V. Pandit, *Mater. Today: Proc.*, 2021, **52**, 17–20.

40 W. Gu, X. Huang, Y. Tian, M. Cao, L. Zhou, Y. Zhou, J. Lu, J. Lei, Y. Zhou, L. Wang, Y. Liu and J. Zhang, *Appl. Surf. Sci.*, 2021, **538**, 147813.

41 J. Sun, X. Yan, K. Lv, S. Sun, K. Deng and D. Du, *J. Mol. Catal. A: Chem.*, 2013, **367**, 31–37.

42 K. Kumar, R. P. Dave, S. Dev and M. Singh, *RSC Adv.*, 2022, **12**, 29734–29756.

43 R. K. Singh, R. Kumar and D. P. Singh, *RSC Adv.*, 2016, **6**, 64993–65011.

44 C. Liu, Z. Yu, D. Neff, A. Zhamu and B. Z. Jang, *Nano Lett.*, 2010, **10**, 4863–4868.

45 M. Sun, J. Ma, M. Zhang, Y. Xiao, Y. Zhu and S. Zhang, *Mater. Chem. Phys.*, 2020, **241**, 122450.

46 K. Kumar, B. Sahoo, T. Chand Meghwal and M. Singh, *Energy Adv.*, 2023, **2**, 198–225.

47 T. Wang, B. R. Li, L. G. Wu, Y. B. Yin, B. Q. Jiang and J. Q. Lou, *Adv. Powder Technol.*, 2019, **30**, 1920–1931.

48 K. Kumar and M. Singh, *RSC Adv.*, 2025, 6593–6633.

49 D. Hao, Y. X. Song, Y. Zhang and H. T. Fan, *Appl. Surf. Sci.*, 2021, **543**, 148810.

50 V. U. Pandit, S. S. Arbuj, U. P. Mulik and B. B. Kale, *Environ. Sci. Technol.*, 2014, **48**, 4178–4183.

51 V. Jawale, G. Gugale, M. Chaskar, S. Pandit, R. Pawar, S. Suryawanshi, V. Pandit, G. Umarji and S. Arbuj, *J. Mater. Res.*, 2021, **36**, 1573–1583.

52 K. Kumar, B. Sahoo, T. C. Meghwal and M. Singh, *Energy Adv.*, 2023, **3**, 198–225.

53 S.-J. Zou, Y.-F. Chen, Y. Zhang, X.-F. Wang, N. You and H.-T. Fan, *J. Alloys Compd.*, 2021, **863**, 158475.

54 Z. Quan, Z. Wang, P. Yang, J. Lin and J. Fang, *Inorg. Chem.*, 2007, **46**, 1354–1360.

55 H. Wu, L. Li, K. Chang, K. Du, C. Shen, S. Zhou, G. Sheng, W. Linghu, T. Hayat and X. Guo, *J. Environ. Chem. Eng.*, 2020, **8**, 103882.

56 S. Dev and M. Singh, *J. Phys. Chem. Solids*, 2020, **139**, 109335.

57 I. L. Ikhioya and A. C. Nkele, *Arabian J. Sci. Eng.*, 2023, **49**, 1217–1225.

58 A. Deptula, M. Wade, S. A. Rogers and R. M. Espinosa-marzal, *Adv. Funct. Mater.*, 2022, 2111414.

59 J. Dadashi, M. A. Ghasemzadeh and M. Salavati-Niasari, *RSC Adv.*, 2022, **12**, 23481–23502.

60 C. Wang, M. Chen, J. Wu, F. Mo and Y. Fu, *Anal. Chim. Acta*, 2019, **1086**, 66–74.

61 P. Borthakur and M. R. Das, *J. Colloid Interface Sci.*, 2018, **516**, 342–354.

62 S. Fentie Tadesse, D. H. Kuo, W. Lakew Kebede and G. Sisay Wolde, *Appl. Surf. Sci.*, 2021, **569**, 151091.